Tunable Multi-Functional Metamaterial Based on Photosensitive Silicon for Unidirectional Reflectionlessness, Polarization Conversion and Asymmetric Transmission

Xue Ren , Yi Wen Zhang , Ying Qiao Zhang * , Xing Ri Jin *

Posted Date: 22 April 2025

doi: 10.20944/preprints202504.1857.v1

Keywords: unidirectional reflectionlessness; polarization conversion; asymmetric transmission; metamaterial

 doi:10.20944/preprints202504.1857.v1

Article

Tunable Multi-Functional Metamaterial Based on Photosensitive Silicon for Unidirectional Reflectionlessness, Polarization Conversion and Asymmetric Transmission

Xue Ren, Yi Wen Zhang, Ying Qiao Zhang * and Xing Ri Jin *

Department of Physics, College of Science, Yanbian University, Yanji, Jilin 133002, China
* Correspondence: yqzhang@ybu.edu.cn (Y.Q.Z.); xrjin@ybu.edu.cn (X.R.J.)

Abstract: We propose a tunable multi-functional metamaterial composed of two pairs of gold corner resonators interconnected with photosensitive silicon, operating in the terahertz range. This design achieves dual-band unidirectional reflectionlessness, polarization conversion, and asymmetric transmission for linearly polarized waves, regardless of whether the photosensitive silicon is in its insulating or metallic state. When photosensitive silicon transitions from the insulating state to metallic state, its conductivity increases significantly, resulting in a frequency shift phenomenon in the functional peak frequencies. Numerical simulations demonstrate the structure's robust performance in dual-band unidirectional reflectionlessness and significant asymmetric transmission, with minimal sensitivity to variations in the incident angle and photosensitive silicon sheet length. By integrating multiple functionalities and enabling frequency tunability through photosensitive silicon conductivity control, this design offers a reconfigurable solution for THz applications such as switches, polarization converters and modulators.

Keywords: unidirectional reflectionlessness; polarization conversion; asymmetric transmission; metamaterial

1. Introduction

Terahertz (THz) waves, spanning the frequency range of 0.1 THz to 10 THz, occupy the transitional region of macroscopic electronics and microscopic photonics within the electromagnetic spectrum, which makes the boundary between microwaves and infrared radiation[1–3]. THz waves exhibit exceptional properties, including a broad bandwidth, high penetration efficiency, low photon energy and strong coherence[4–7]. However, the lack of functional materials that can efficiently interact with THz waves has severely limited their practical applications, as most natural materials show only weak interactions in this frequency range. In this context, metamaterials have emerged as a promising solution. They are artificially engineered periodic structures made of subwavelength unit cells, enabling unique control over THz waves[8–10]. At specific THz frequencies, metamaterials exhibit unique physical properties that are unattainable with traditional materials, such as negative refraction[11], electromagnetic invisibility[12–14], and electromagnetic shielding[15]. As research in this field progresses, precise control over the amplitude, phase and polarization of electromagnetic waves has become achievable through the meticulous design of the shape, size and arrangement of the unit cells within metamaterials[16,17]. Moreover, metamaterials have been instrumental in the design and fabrication of optical devices with advanced functionalities, including unidirectional reflectionlessness(UR)[18–20], polarization conversion(PC)[21] and asymmetric transmission(AT)[22–24]. For instance, a metamaterial composed of double-layer double i-shaped resonators has been proposed, enabling control over UR and AT by adjusting the angle of incidence[25]. In the THz regime, a broadband bi-functional metasurface combining a double split ring resonator with a bar resonator has been designed to significantly enhance the bandwidth and efficiency of PC and AT[26]. Additionally,

 doi:10.20944/preprints202504.1857.v1

an ultra-broadband multilayer metasurface, resembling a Fabry-Perot cavity, has demonstrated ultra-broadband cross-polarization conversion and efficient AT, with both functionalities remaining stable at an incidence angle of 0°∼45°[27]. However, once the geometric parameters of these structures are fixed, their performance becomes unchanging. To overcome this limitation, researchers have integrated tunable materials into metamaterials, thereby combining tunability with multifunctionality[28].

For tunable THz metamaterials, their key to achieve the tunability lies in utilizing active materials to modulate conductivity[29]. So far, three typical active materials have emerged for tunable THz metamaterials: vanadium dioxide (VO_2)[30–33], graphene[34–36] and photosensitive silicon (PSi)[37–39]. PSi enables fast optical tuning without thermal constraints, unlike VO_2 and offers easier fabrication compared to graphene's complex doping requirements[40,41]. In contrast, PSi has been widely recognized owing to its conductivity modulation mechanism, where the conductivity can be tuned by adjusting the intensity of the pump beam[42]. The tunable metamaterial has been demonstrated based on silicon state modulation[43]. In the insulating state, the metamaterial has achieved a polarization conversion ratio (PCR) exceeding 0.9 within 3.82 THz to 4.43 THz, while in the metallic state, it exhibits broadband absorption from 1.45 THz to 3.36 THz. Besides, a dual-frequency switch utilizing PSi has been developed[40], where the conductivity has been modulated by varying the pump beam intensity to enable switching between on and off states. Up to now, although numerous designs of multifunctional metamaterials have been proposed, achieving metamaterials that simultaneously possess tunability, UR, PC and AT optical properties remain a significant challenge.

In this study, we propose a tuanble multi-functional THz metamaterial based on PSi that integrates UR, PC and AT for linearly polarized waves. When PSi acts as an insulator with the conductivity of 1 S/m, the structure demonstrates dual-band UR and PC capabilities, exhibiting the higher PCRs for both x- and y-polarized waves. Conversely, when PSi is metallic state with the conductivity of 1×10^5 S/m, the metamaterial achieves all desired functionalities across a broader frequency range, accompanied by frequency shifts in UR, PC and AT. Additionally, there are better AT parameters for both x- and y-polarized waves. That highlights the versatility, superior performance and adjustability of the design.

2. Structure Design and Methods

Figure 1 illustrates the geometric configuration and dimensional specifications of the proposed metamaterial unit cell, featuring a composite structure of PSi integrated with two pairs of gold corner resonators. Figure 1a depicts its unit cell configuration that comprises a SiO_2 substrate with the dielectric constant of 2.07[44]. The polyimide dielectric layer, characterized by a dielectric constant of 2.4 and a loss tangent of 0.005, encapsulates two pairs of gold corner resonators integrated with PSi. Figures 1b and 1c present the front views of the lower and upper resonators, respectively. As depicted in Figure 1b, the unit cell exhibits a periodicity of P = 100 μm, while the metallic corner resonators are characterized by the following geometric parameters: outer side length R = 44 μm, inner side length r = 30 μm, resonator width w = 14 μm and PSi length b = 4 μm. The two pairs of metallic corner resonators are geometrically identical and symmetrical about the central point O. The upper resonator is generated by rotating the lower one counterclockwise by an angle of α = 40°, as illustrated in Figure 1c. Figure 1d presents a side view of the unit cell in y-z plane, illustrating the layered structure with precise dimensional parameters. The substrate thickness (t_1) measures 10 μm, while the resonator and dielectric layer have thicknesses of t_2 = 0.2 μm and s = 30 μm, respectively. Additionally, the vertical separation distance (h) between the upper and lower resonators is maintained at 20 μm. Numerical simulations are conducted using CST Microwave Studio, employing the frequency-domain finite integration technique. The boundary conditions are configured with unit cell periodicity along both the x- and y-axes, while an open boundary condition is applied in the z-axis. In the simulation, the conductivity of gold is set to 4.561×10^7 S/m, while the dielectric constant of PSi is assigned a value of 11.9[45]. Moreover, its conductivity demonstrates a dynamic dependence on the power of the applied optical pump beam. Under illumination by a near-infrared

 doi:10.20944/preprints202504.1857.v1

laser pulse centered at 800 nm, which serves as the optical pump for carrier generation in PSi, the conductivity of PSi varies with the incident energy flux. This relationship can be mathematically expressed as: $\sigma_{PSi} = 4.863\times10^{-4}\times I^2+0.1856\times I+1.569$[46], where σ_{PSi} denotes the conductivity of PSi and I represents the pump beam power. In the absence of optical pumping (I = 0), the conductivity of PSi measures approximately 1 S/m. However, when subjected to a pump beam power of 294.6 μJ/cm^2, the conductivity undergoes a significant enhancement, reaching approximately 1×10^5 S/m.

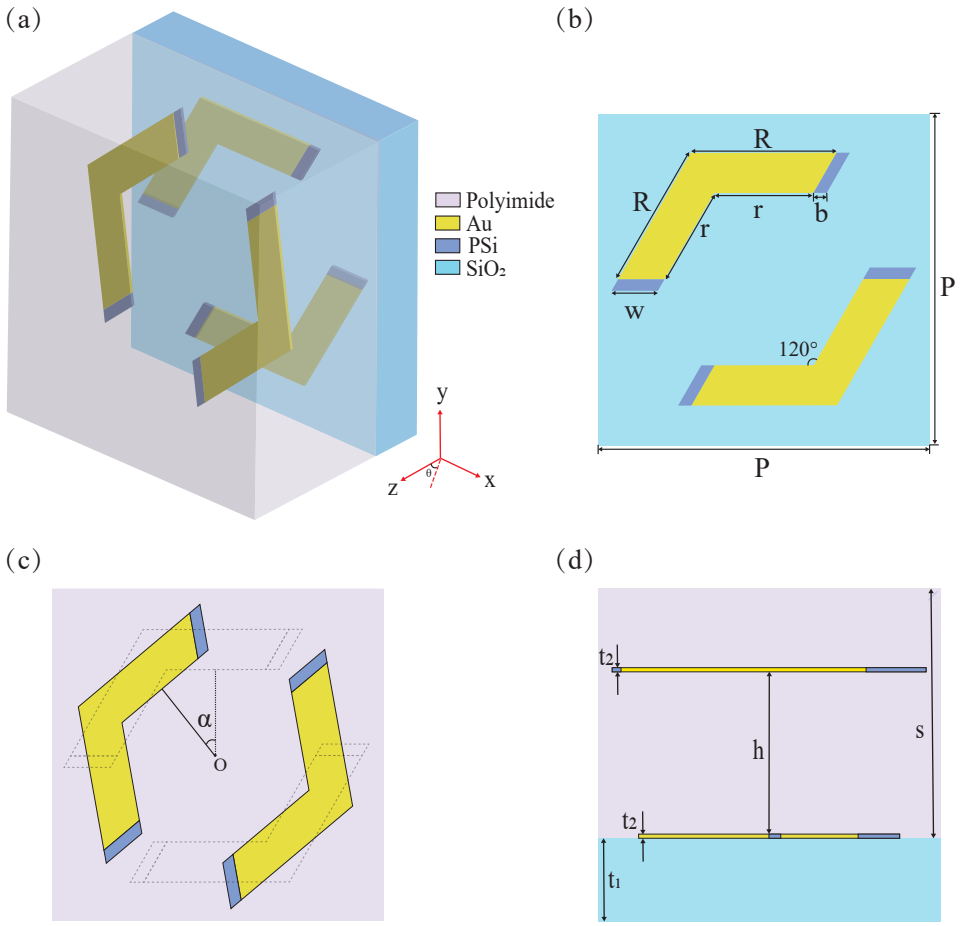

Figure 1. (a) Unit cell diagram of metamaterial. (b) Front view of the lower resonator. (c) Front view of the upper resonator. (d) Side view of the unit cell in the y-z plane.

To facilitate the analysis of the reflection and transmission characteristics of electromagnetic waves in structure, we use Jones matrix to establish the relationships between the incident field and reflected field as well as the transmitted field[47]

$$E_i(r,t) = \begin{pmatrix} I_x \\ I_y \end{pmatrix} e^{i(kz-wt)}, \tag{1}$$

$$E_r(r,t) = \begin{pmatrix} r_x \\ r_y \end{pmatrix} e^{i(kz-wt)}, \tag{2}$$

$$E_t(r,t) = \begin{pmatrix} t_x \\ t_y \end{pmatrix} e^{i(kz-wt)}, \tag{3}$$

 doi:10.20944/preprints202504.1857.v1

where ω represents the angular frequency of the incident wave, and k denotes the wave vector. The complex amplitudes of the incident wave along the x- and y- directions are given by I_x and I_y, respectively. Correspondingly, r_x and r_y signify the complex amplitudes of the reflected wave in the x- and y- directions, while t_x and t_y represent those of the transmitted wave, respectively. Additionally, the Jones matrices utilized to characterize the relationships between the transmitted wave, reflected wave and the incident linearly polarized wave can be expressed as

$$\begin{pmatrix} t_x \\ t_y \end{pmatrix} = \begin{pmatrix} t_{xx} & t_{xy} \\ t_{yx} & t_{yy} \end{pmatrix} \begin{pmatrix} I_x \\ I_y \end{pmatrix} = T^f_{lin} \begin{pmatrix} I_x \\ I_y \end{pmatrix}, \tag{4}$$

$$\begin{pmatrix} r_x \\ r_y \end{pmatrix} = \begin{pmatrix} r_{xx} & r_{xy} \\ r_{yx} & r_{yy} \end{pmatrix} \begin{pmatrix} I_x \\ I_y \end{pmatrix} = R^f_{lin} \begin{pmatrix} I_x \\ I_y \end{pmatrix}, \tag{5}$$

where, the subscript "lin" refers to linearly polarized wave, and the superscript "f" indicates forward ($-z$) incidence. The terms t_{xx} (t_{yy}) and r_{xx} (r_{yy}) represent the transmitted and reflected waves in the x (y)-direction when the polarization of the incident wave is along the x (y)-direction. Similarly, t_{xy} (t_{yx}) and r_{xy} (r_{yx}) denote the transmitted and reflected waves in the x (y)-direction when the polarization of the incident wave is along the y (x)-direction. Based on the reciprocity theorem, the Jones matrices for backward ($+z$) propagation can be expressed as follows

$$T^b_{lin} = \begin{pmatrix} t_{xx} & -t_{yx} \\ -t_{xy} & t_{yy} \end{pmatrix}, \tag{6}$$

$$R^b_{lin} = \begin{pmatrix} r_{xx} & -r_{yx} \\ -r_{xy} & r_{yy} \end{pmatrix}. \tag{7}$$

So, the total transmissions and reflections of x- and y-polarized incident waves along the forward and backward directions can be written as, respectively,

$$T^{f(b)}_{x(y)} = \left| t^{f(b)}_{xx(yy)} \right|^2 + \left| t^{f(b)}_{yx(xy)} \right|^2, \tag{8}$$

$$R^{f(b)}_{x(y)} = \left| r^{f(b)}_{xx(yy)} \right|^2 + \left| r^{f(b)}_{yx(xy)} \right|^2. \tag{9}$$

In addition, the performance of metamaterial in PC is characterized by the PCR, defined as follows[48]

$$\mathrm{PCR}^f = \frac{|t_{yx}|^2}{|t_{yx}|^2 + |t_{xx}|^2}, \tag{10}$$

$$\mathrm{PCR}^b = \frac{|t_{xy}|^2}{|t_{xy}|^2 + |t_{yy}|^2}. \tag{11}$$

Besides, AT effect of the metamaterial can be characterized by the AT parameter $\triangle$. This parameter quantifies the difference in total transmissions for the same polarized wave between the forward and backward directions and that for polarized waves can be derived directly from the Jones matrix, as

$$\Delta^x_{lin} = T^f_x - T^b_x = |t^f_{xx}|^2 + |t^f_{yx}|^2 - |t^b_{xx}|^2 - |t^b_{yx}|^2, \tag{12}$$

$$\Delta^y_{lin} = T^f_y - T^b_y = |t^f_{yy}|^2 + |t^f_{xy}|^2 - |t^b_{yy}|^2 - |t^b_{xy}|^2 = -\triangle^x_{lin}. \tag{13}$$

 doi:10.20944/preprints202504.1857.v1

3. Results and Discussion

3.1. Unidirectional reflectionlessness

Figure 2a,b show the co-polarized reflection spectra for forward and backward directions under x- and y-polarized waves, respectively. In these figures, the dash-dotted and solid lines correspond to the cases of the insulating ($\sigma_{\mathrm{PSi}} = 1$ S/m) and metallic ($\sigma_{\mathrm{PSi}} = 1\times10^5$ S/m) states of PSi, with color-coded representations: blue (black) and green (red) dash-dotted (solid) lines indicate forward and backward reflections in insulating (metallic) state of PSi, respectively, for x- and y-polarized waves. For x-polarized wave (Figure 2a), the insulating state of PSi demonstrates co-polarized reflection R^b_{xx} of approximately 0.69 and 0.59 at 1.27 THz and 1.79 THz (green dash-dotted line) where R^f_{xx} remains near zero (blue dash-dotted line), respectively. In the metallic state of PSi, R^b_{xx} value reaches about 0.71 and 0.51 at 1.06 THz and 1.71 THz (red solid line), with R^f_{xx} maintaining near-zero (black solid line), clearly indicating the dual-band UR phenomenon for x-polarized wave. Regarding y-polarized wave (Figure 2b), the insulating state of PSi shows co-polarized reflection R^f_{yy} of approximately 0.75 and 0.61 at 1.26 THz and 1.86 THz (blue dash-dotted line) where R^b_{yy} approaches zero (green dash-dotted line), respectively. In the metallic state of PSi, R^f_{yy} value increases to about 0.80 and 0.65 at 1.05 THz and 1.76 THz (black solid line), with R^b_{yy} remaining nearly zero (red solid line), confirming the dual-band UR phenomenon for y-polarized wave. These observations demonstrate that the UR phenomenon can be effectively modulated through PSi state transitions, exhibiting the distinct red shift behavior when PSi changes from insulating to metallic state. Therefore, the structure exhibits robust dual-band UR characteristic.

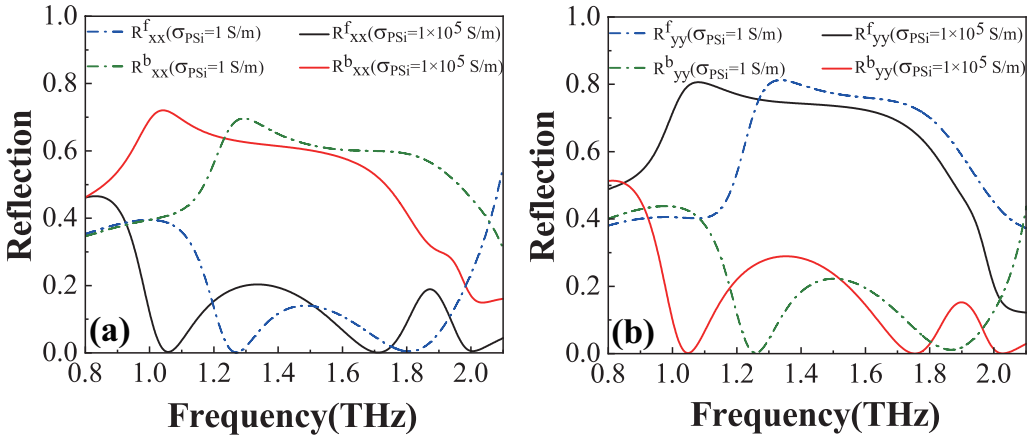

Figure 2. The co-polarized reflections for x-polarized wave(a) and y-polarized wave(b), respectively, for forward and backward directions when PSi is in insulating state or metallic state.

To gain deeper insights into the generation mechanism of UR, the z-component electric field distributions are presented in Figures 3 and 4 for PSi in the insulating state. For conciseness, the analysis focuses solely on the electric field distributions of x- and y-polarized waves in the insulating state of PSi. Figure 3 illustrates the electric field distributions of the upper and lower resonators for the x-polarized wave at frequencies of 1.27 THz and 1.79 THz, respectively. As shown in Figures 3a$_1$ and 3a$_2$, at 1.27 THz, when the x-polarized wave is incident in the forward direction, both the upper and lower resonators are strongly excited with a phase difference approaching π, leading to the near-zero reflection (Figure 2a blue dash-dotted line) due to destructive interference. Conversely, Figures 3b$_1$ and 3b$_2$ reveal that, for backward incidence, the upper resonator is weakly excited while the lower resonator is strongly excited, resulting in a high reflection of ∼0.69 (Figure 2a green dash-dotted line). A similar behavior is observed at 1.79 THz, as depicted in Figures 3c$_1$–3d$_2$, confirming the UR phenomenon at this frequency. In contrast, for the y-polarized wave, the excitation characteristics differ significantly. As demonstrated in Figures 4a$_1$–4d$_2$, in the forward direction, the upper resonator is strongly excited while the lower resonator is weakly excited, yielding high reflection of ∼0.75 and ∼0.61 at 1.26 THz and 1.86 THz, respectively (Figure 2b blue dash-dotted line). However, in

 doi:10.20944/preprints202504.1857.v1

the backward direction, both resonators are strongly excited with the phase difference close to π, resulting in near-zero reflection at these frequencies (Figure 2b green dash-dotted line). Through detailed analysis of the electric field distributions, the dual-band UR phenomenon is clearly observed, highlighting the critical role of resonator excitations and phase difference in achieving UR.

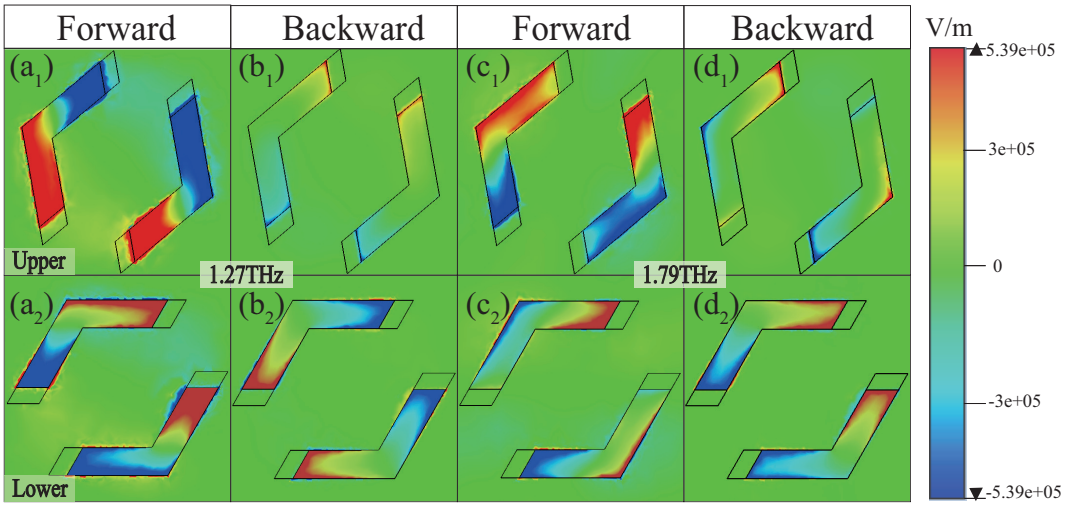

Figure 3. The z-component electric field distributions for the upper (a_1) - (d_1) and lower (a_2) - (d_2) resonators at 1.27 THz and 1.79 THz for x-polarized wave along the forward and backward directions, respectively.

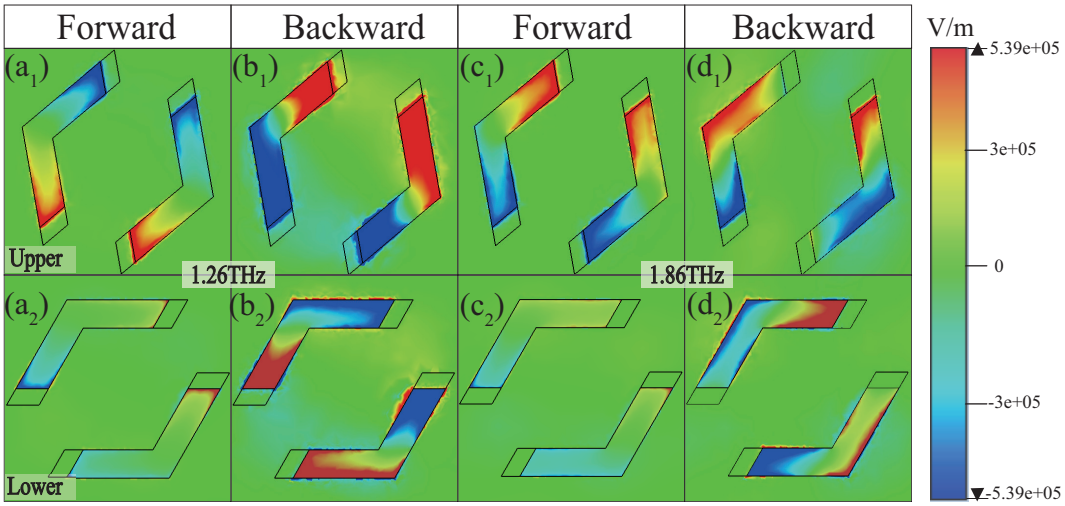

Figure 4. The z-component electric field distributions for the upper (a_1) - (d_1) and lower (a_2) - (d_2) resonators at 1.26 THz and 1.86 THz for y-polarized wave along the forward and backward directions, respectively.

3.2. Polarization Conversion

Next, we analyze the PC characteristics of the transmission waves in both forward and backward directions for x- and y-polarized incident waves, as illustrated in Figure 5. From Figures 5a and 5c, it is observed that when PSi is in the insulating state, the cross-polarized transmission T^b_{xy} exceeds 0.6 within the frequency ranges of 1.22 THz∼1.39 THz and 1.64 THz∼1.90 THz, while, in the corresponding frequeny ranges, the transmissions T^f_{yy}, T^f_{xy} and T^b_{yy} remain below 0.20. In contrast, when PSi is in the metallic state, T^b_{xy} surpasses 0.6 in the frequency ranges of 1.02 THz∼1.12 THz and 1.67 THz∼1.70 THz, while, in the corresponding frequeny ranges, the transmissions T^f_{yy}, T^f_{xy} and T^b_{yy} remain below 0.20. This demonstrates that a y-polarized wave incident in the backward direction is predominantly converted into an x-polarized wave. Similarly, from Figures 5b and 5d, it is evident that the cross-polarized transmission T^f_{yx} exceeds 0.6 in the frequency ranges of 1.22 THz∼1.39 THz and 1.66 THz∼1.92 THz for the forward direction when PSi is in the insulating state, while, in the corresponding frequeny ranges, the transmissions T^b_{yx}, T^b_{xx} and T^f_{xx} all remain below 0.2. When PSi is in the metallic state,

 doi:10.20944/preprints202504.1857.v1

T^f_{yx} exceeds 0.6 in the frequency ranges of 1.02 THz∼1.12 THz and 1.67 THz∼1.70 THz, while, in the corresponding frequeny ranges, the transmissions T^b_{yx}, T^b_{xx} and T^f_{xx} all remain below 0.2. This indicates that an x-polarized wave incident in the forward direction is predominantly converted into a y-polarized wave. These results highlight that the proposed structure not only achieves efficient PC but also exhibites exceptional AT performance.

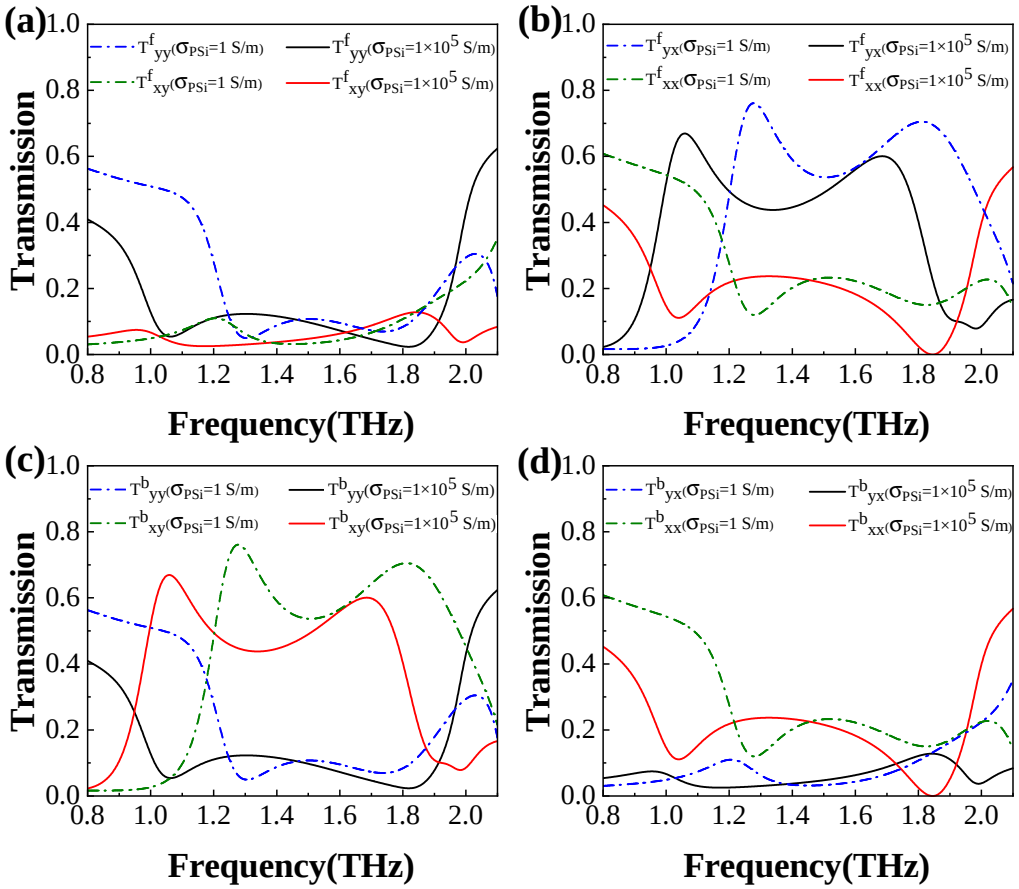

Figure 5. The transmission characteristics of linearly polarized waves for both insulating and metallic states of PSi. The transmission spectra of y-polarized wave incident in the forward (a) and backward (c) directions, as well as x-polarized wave incident in the forward (b) and backward (d) directions.

The PCR is a critical parameter for evaluating the PC capability, as Equations (10) and (11) define. The transmission PCR curves versus frequency for both insulating and metallic states of PSi are illustrated in Figures 6a and 6b for the forward and backward directions, respectively, when x- and y-polarized waves are incident. As shown in Figure 6a, when x-polarized wave propagates in the forward direction with PSi in the insulating state, the PCR_x value exceeds 0.8 within the frequency ranges of 1.23 THz∼1.35 THz and 1.74 THz∼1.88 THz. The peak value of PCR_x reach approximately 0.86 and 0.82 at 1.28 THz and 1.82 THz, respectively. When PSi is in the metallic state, the PCR_x value for the frequency ranges of 1.00 THz∼1.10 THz and 1.66 THz∼1.88 THz also surpasses 0.8, with peak values of approximately 0.86 and 0.99 at 1.04 THz and 1.84 THz, respectively. Similarly, for y-polarized wave incident in the backward direction with PSi in the insulating state (Figure 6b), the PCR_y values exceed 0.9 within the frequency ranges of 1.26 THz∼1.36 THz and 1.70 THz∼1.78 THz. The peak PCR_y reach approximately 0.94 and 0.90 at 1.30 THz and 1.74 THz, respectively. When PSi is in the metallic state, the PCR_y value for the frequency ranges of 1.03 THz∼1.10 THz and 1.63 THz∼1.84 THz also exceeds 0.9, with peak values of approximately 0.93 and 0.94 at both 1.06 THz and 1.78 THz, respectively. These results clearly demonstrate that when the x (y)-polarized wave propagates in the forward (backward) direction, the majority of the x (y)-polarized wave is converted into the y (x)-polarized wave. These findings confirm that the designed metamaterial exhibits well PC capability.

 doi:10.20944/preprints202504.1857.v1

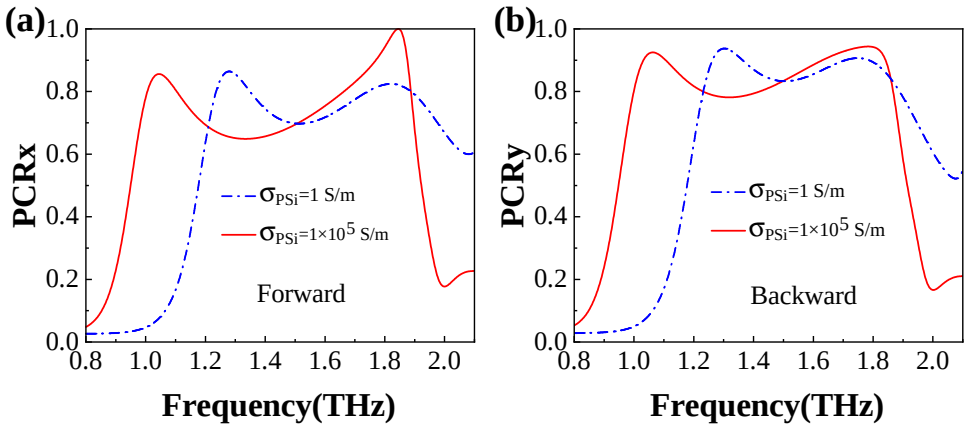

Figure 6. The PCR$_x$ for forward (a) and PCR$_y$ for backward (b) directions, respectively, with PSi in the insulating and metallic states.

3.3. Asymmetric Transmission

In the following, the AT parameter curves, denoted as Δ, are plotted in Figure 7 based on Equations (12) and (13) for both insulating and metallic states of PSi. Notably, the AT parameters Δ display entirely opposite trends for x- and y-polarized waves. Specifically, when PSi is in the insulating (metallic) state, the values of Δ_{lin}^{x} are approximately 0.69 (0.63) and 0.60 (0.52) at frequencies of 1.29 THz (1.06 THz) and 1.77 THz (1.67THz), respectively, while the corresponding values of Δ_{lin}^{y} are approximately -0.69 (-0.63) and -0.60 (-0.52). These findings demonstrate that the AT effect can be effectively achieved for both x- and y-polarized waves, underscoring the polarization-independent AT characteristics of the structure.

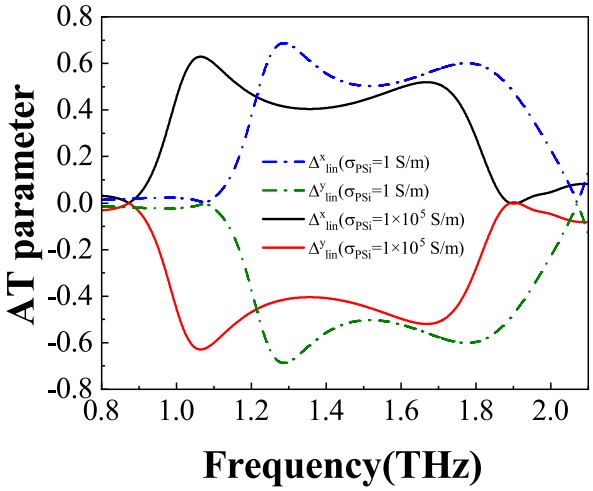

Figure 7. The AT parameters of x- and y-polarized incident waves under insulating and metallic states of PSi.

3.4. The Effect of Incident Angle and PSi Sheet Length on UR and AT

To investigate the influences of the incident angle θ and the length b of the PSi sheet on UR, we plot the co-polarized reflections of the linearly polarized incident waves as the functions of the incident angle θ and the length b of the PSi sheet, respectively. Figure 8a–d illustrate the co-polarized reflections for forward and backward directions of the x- and y-polarized waves versus incident angle θ and frequency when PSi is in the insulating state. As shown in Figure 8a (8d), the co-polarized reflection $R_{xx}^{f}(R_{yy}^{b})$ approaches nearly zero around 1.27 THz (1.26 THz) and 1.79 THz (1.86 THz) within the incident angle range of $0°\sim45°$, which correspond to high reflection $R_{xx}^{b}(R_{yy}^{f})$ in Figure 8b (8c). From Figures 8a-8d, it is evident that dual-band UR phenomena occur for both x- and y-polarized waves, respectively. Similarly, when PSi is in the metallic state, as shown in Figures 8e and 8f, the co-polarized reflection R_{xx}^{f} approaches nearly zero around frequencies of 1.06 THz and 1.71 THz within the incident

 doi:10.20944/preprints202504.1857.v1

angle range of 0°∼45°, while R_{xx}^{b} exhibits relatively high reflection. In Figures 8g and 8h, around frequencies of 1.05 THz and 1.76 THz, the co-polarized reflection R_{yy}^{b} approaches nearly zero within the incident angle range of 0°∼45°, while R_{yy}^{f} exhibits relatively high reflection. These results demonstrate that the proposed structure exhibits dual-band UR phenomena over the wide ranges of incident angle.

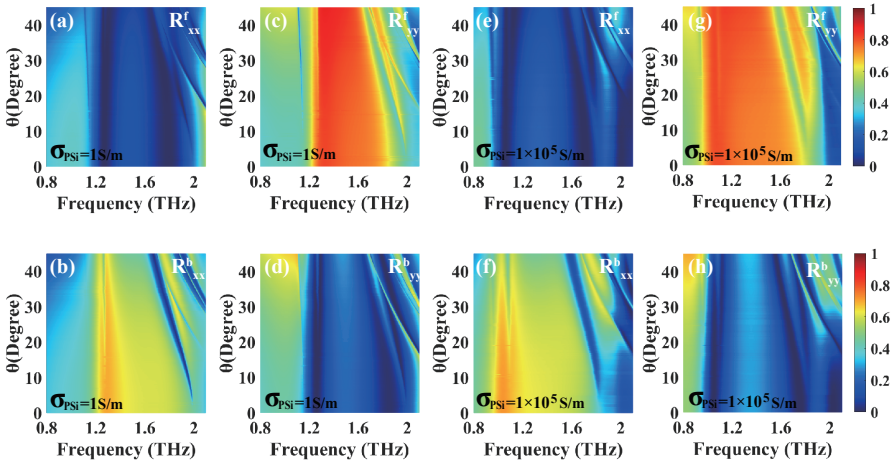

Figure 8. The dependences of co-polarized reflections of the linearly polarized incident waves on the incident angle θ and frequency for both forward and backward directions when PSi is in insulating state (a-d) and metallic state (e-h), respectively, in the case of PSi sheet length b=4 μm.

The co-polarized reflection spectra of x- and y-polarized waves for both forward and backward directions are presented in Figure 9, respectively, showing the dependences on the length b of the PSi sheet for both insulating and metallic states. As depicted in Figures 9a-9d, when PSi is in the insulating state, the co-polarized reflection R_{xx}^{b} (R_{yy}^{f}) remains consistently high and stable at frequencies of 1.27 THz (1.26 THz) and 1.79 THz (1.86THz) as the length b of the PSi sheet increases from 3.5 μm to 4.5 μm. In contrast, the co-polarized reflection R_{xx}^{f} (R_{yy}^{b}) approaches nearly zero at the same frequencies. Similarly, when PSi is in the metallic state, as illustrated in Figures 9e-9h, the co-polarized reflection R_{xx}^{b} (R_{yy}^{f}) demonstrates high stability at frequencies of 1.06 THz (1.05 THz) and 1.71 THz (1.76 THz) with increasing the length b of the PSi sheet from 3.5 μm to 4.5 μm, while R_{xx}^{f} (R_{yy}^{b}) approaches nearly zero at the same frequencies. From Figures 9a–9h, it is concluded that the structure exhibits dual-band UR over a wide range of PSi sheet length, and the peak positions of UR exhibiting the slight red shift.

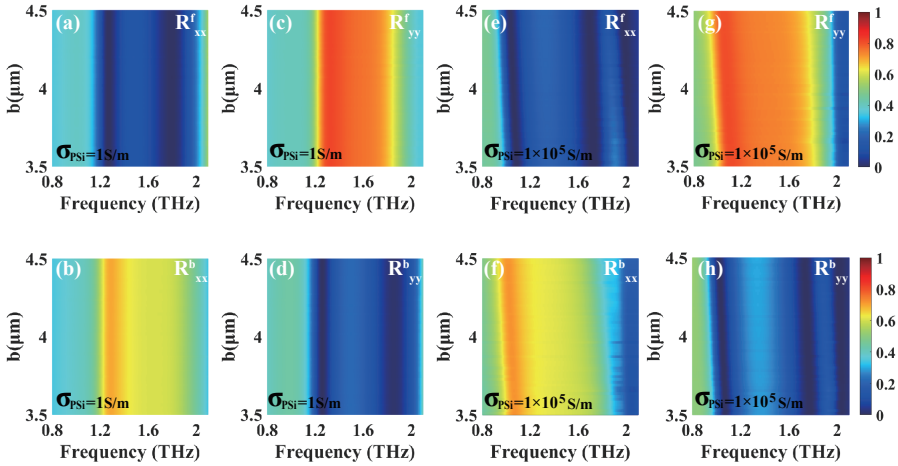

Figure 9. The dependences of co-polarized reflections on the length b of the PSi sheet and frequency for both forward and backward directions when PSi is in insulating state (a-d) and metallic state (e-h), respectively, in the case of incident angle θ=0°.

 doi:10.20944/preprints202504.1857.v1

Finally, we investigats the AT parameter by varying the incidence angle θ and the length b of the PSi sheet, respectively, with Figure 10 presenting a comprehensive analysis of its variations under different conditions. In the insulating state of PSi, the AT parameter demonstrates distinct characteristics across different frequencies. As shown in Figure 10a, the AT parameter maintains stable values of ∼0.69 and ∼0.60 around the frequencies of 1.29 THz and 1.77 THz when the incident angle θ is in the ranges of 0°∼45° and 0°∼26°, respectively, with b fixed at 4 μm. Furthermore, Figure 10c reveals that when the PSi sheet length b is varied from 3.5 μm∼4.5 μm, the AT parameter exhibits remarkable stability at values of ∼0.69 and ∼0.60 around the frequencies of 1.29 THz and 1.77 THz, respectively, with incidence angle θ = 0°. When PSi is in the metallic state, the AT parameter behavior undergoes significant changes, maintaining stable values of ∼0.63 at 1.06 THz and ∼0.52 at 1.67 THz as the incident angle θ increases from 0°∼45° and 0°∼19° with b fixed at 4 μm (Figure 10b), respectively. when the PSi sheet length b varies from 3.5 μm∼4.5 μm at θ = 0° (Figure 10d), the AT parameter remaining ∼0.63 and ∼0.52 unchanged around 1.06 THz and 1.67 THz. Obviously, the AT parameter in the insulating state consistently exhibits the higher values compared to metallic state, and the transition to the metallic state induces the red shifts with peak values of AT parameter. Notably, the AT parameter demonstrates remarkable stability to variations over the wide ranges of the incident angle and PSi sheet length.

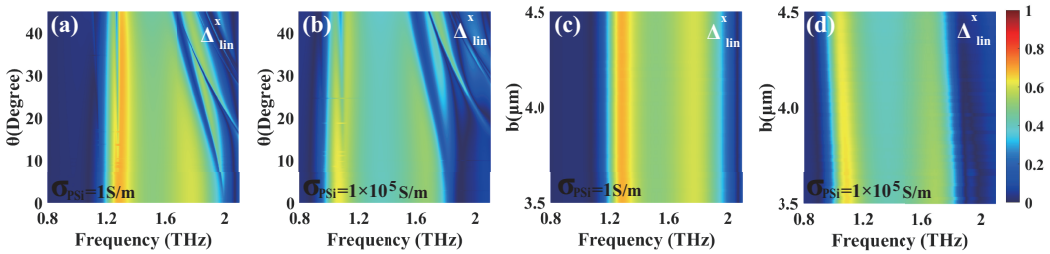

Figure 10. AT parameter Δ_{lin}^{x} varied with the incident angle θ ((a),(b)) and the length b of PSi sheet ((c),(d)) in insulating ((a),(c)) and metallic ((b),(d)) states of PSi, respectively, when the length b=4 μm and incident angle θ=0°.

3.5. Relative Advantages and Potential Fabrication Processes

Compared with the existing literature summarized in Table 1 [49–54], the proposed structure exhibits significant advantages: it simultaneously achieves UR, PC and AT, while supporting dynamic tuning and enabling red shift of their peak frequencies. Moreover, the structure demonstrates robust performance against variations in the wider ranges of the incident angle and PSi sheet length. These findings provide new insights for the design of multifunctional optical devices, highlighting their broad technological potential.

Table 1. Comparison with other functional devices.

References	Incident light type	Tunable material	Function	PC type	Spectrum range	Frequency shift
[47]	LPL	PSi,VO_2	PC, LTCPC	R,T	THz	No
[48]	LPL	PSi,Graphene	T,A,R	No	THz	No
[49]	LPL	PSi,VO_2	PC,A	T	THz	No
[50]	CPL	PSi	CDR,CDT	No	THz	No
[51]	LPL	PSi	EIT	No	THz	No
[52]	LPL	PSi	A	No	THz	Red-shift, Blue-shift
This work	LPL	PSi	UR,PC,AT	T	THz	Red-shift

* Explanation of abbreviations: LPL: linearly polarized light, CPL: circularly polarized light, LTCPC: linear to circular polarization conversion, R: reflection, T: transmission, A: absorption, CDR: circular dichroism of reflection, CDT: circular dichroism of transmission, EIT: electromagnetically induced transparency.

 doi:10.20944/preprints202504.1857.v1

Next, we outline the fabrication processes for the proposed structure. According to Ref.[55], the metamaterial can be fabricated using conventional lithography technique. Initially, a photoresist layer is spin-coated and deposited onto the substrate. Gold corner resonators are then patterned via photolithography and lift-off processes[56], while the PSi layer is prepared using photolithography combined with high-power magnetron pulsed sputtering. Subsequently, a dielectric material is deposited onto the first layer. By repeating these steps, a second resonator can be fabricated. As supported by the previous study[48], the proposed structure is feasible to fabricate under the current technical conditions.

4. Conclusions

We design a tunable THz multifunctional metamaterial using the metal corner resonators connected with PSi, which integrates three key functionalities-unidirectional reflectionlessness, polarization conversion and asymmetric transmission-in one. Remarkably, regardless of whether the PSi is in the insulating or metallic state, the structure supports dual-band unidirectional reflectionlessness and polarization conversion for x- (y-) polarized wave, reaching polarization conversion ratio PCR_x (PCR_y) of up to 0.86 (0.94) for insulating state and 0.99 (0.93) for metallic state, while maintains the higher AT parameters. The phase transition of PSi from insulating to metallic states enables tunability of peak frequencies, accompanied by the slight red shift. Furthermore, the structure exhibits robust unidirectional reflectionlessness and asymmetric transmission performances over broad incident angle ($0^\circ \sim 45^\circ$) and the PSi sheet length (3.5 μm$\sim$4.5 μm), demonstrating its exceptional performance stability and structural robustness. To summarize, this design overcomes the single-function constraint of traditional metamaterials by integrating unidirectional reflectionlessness, polarization conversion and asymmetric transmission into an unified platform, thereby enabling synergistic control of these functionalities within a single structure. Additionally, the functional peak frequency red shift through control of the conductivity state of PSi opens the possibilities for reconfigurable terahertz switches, polarization converters, modulators and so on.

Author Contributions: Conceptualization, X.R.; simulation, writing - original draft, Y.Z.; supervision, Y.Z. and X.J.; writing - review and editing. X.R., Y.Z., Y.Z. and X.J. All authors have read and agreed to the published version of the manuscript.

Funding: This work is supported by the National Natural Science Foundation of China (Grant No.12064045).

Institutional Review Board Statement: Not applicable.

Informed Consent Statement: Not applicable.

Data Availability Statement: Data Availability Statement: The original contributions presented in this study are included in the article. Further inquiries can be directed to the corresponding author(s).

Acknowledgments: Special thanks to Dexiu Qiu and Wenxuan Yuan for their assistance with the manuscript during the simulation process.

Conflicts of Interest: The authors declare no conflicts of interest.

Abbreviations

The following abbreviations are used in this manuscript:

THz	Terahertz
UR	Unidirectional Reflectionlessness
PC	Polarization Conversion
AT	Asymmetric Transmission
PSi	Photosensitive Silicon
PCR	Polarization Conversion Rate
T	Transmission
R	Reflection
A	Absorption

 doi:10.20944/preprints202504.1857.v1

LPL	Linearly Polarized Light
CPL	Circularly Polarized Light
LTCPC	Linear to Circular Polarization Conversion
CDR	Circular Dichroism of Reflection
CDT	Circular Dichroism of Transmission
EIT	Electromagnetically Induced Transparency

References

1. Xu, C.; Ren, Z.H.; Wei, J.X.; Lee, C.K. Reconfigurable terahertz metamaterials: From fundamental principles to advanced 6G applications. *Iscience* **2022**, *25*, 103799. https://doi.org/10.1016/j.isci.2022.103799.
2. Kumar, A.; Gupta, M.; Pitchappa, P.; Wang, N.; Szriftgiser, P.; Ducournau, G.; Singh, R.J. Phototunable chip-scale topological photonics: 160 Gbps waveguide and demultiplexer for THz 6G communication. *Nat. Commun.* **2022**, *13*, 5404. https://doi.org/10.21979/N9/5FK01V.
3. Aghoutane, B.; El Ghzaoui, M.; El Faylali, H. Spatial characterization of propagation channels for terahertz band. *SN Appl. Sci.* **2021**, *3*, 1–8. https://doi.org/10.1007/s42452-021-04262-8.
4. Jin, Q.; Williams, K.; Dai, J.M.; Zhang, X.C.; et al. Observation of broadband terahertz wave generation from liquid water. *Appl. Phys. Lett.* **2017**, *111*, 071103. https://doi.org/10.1063/1.4990824.
5. Reddy, I.V.K.; Elmaadawy, S.; Furlani, E.P.; Jornet, J.M. Photothermal effects of terahertz-band and optical electromagnetic radiation on human tissues. *Sci. Rep.* **2023**, *13*, 14643. https://doi.org/10.1038/s41598-023-41808-9.
6. Chen, Y.L.; Li, J.Q.; He, C.P.; Qin, J.S.; Chen, X.H.; Li, S.L. Enhancement of high transmittance and broad bandwidth terahertz metamaterial filter. *Opt. Mater.* **2021**, *115*, 111029. https://doi.org/10.1016/j.optmat.2021.111029.
7. Xie, X.; Dai, J.M.; Zhang, X.C. Coherent control of THz wave generation in ambient air. *Phys. Rev. Lett.* **2006**, *96*, 075005. https://doi.org/10.1103/PhysRevLett.96.075005.
8. Lu, Y.L.; Wang, Y. Structural optimization of metamaterials based on periodic surface modeling. *Comput. Methods Appl. Mech. Eng.* **2022**, *395*, 115057. https://doi.org/10.1016/j.cma.2022.115057.
9. Billa, M.B.; Hakim, M.L.; Alam, T.; Almutairi, A.F.; Misran, N.; Soliman, M.S.; Islam, M.T. Near-ideal absorption high oblique incident angle stable metamaterial structure for visible to infrared optical spectrum applications. *Opt. Quantum Electron.* **2023**, *55*, 1115. https://doi.org/10.1007/s11082-023-05412-5.
10. Wei, J.X.; Ren, Z.H.; Lee, C. Metamaterial technologies for miniaturized infrared spectroscopy: Light sources, sensors, filters, detectors, and integration. *J. Appl. Phys.* **2020**, *128*, 240901. https://doi.org/10.1063/5.0033056.
11. Suzuki, T.; Sekiya, M.; Sato, T.; Takebayashi, Y. Negative refractive index metamaterial with high transmission, low reflection, and low loss in the terahertz waveband. *Opt. Express* **2018**, *26*, 8314–8324. https://doi.org/10.1364/OE.26.008314.
12. Manjappa, M.; Pitchappa, P.; Wang, N.; Lee, C.; Singh, R. Active control of resonant cloaking in a terahertz MEMS metamaterial. *Adv. Opt. Mater.* **2018**, *6*, 1800141. https://doi.org/10.1002/adom.201800141.
13. Islam, S.; Hasan, M.; Faruque, M. A new metamaterial-based wideband rectangular invisibility cloak. *Appl. Phys. A* **2018**, *124*, 1–6. https://doi.org/10.1007/s00339-018-1590-9.
14. Wang, B.X.; He, Y.H.; Lou, P.C.; Huang, W.Q.; Pi, F.W. Penta-band terahertz light absorber using five localized resonance responses of three patterned resonators. *Results Phys.* **2020**, *16*, 102930. https://doi.org/10.1016/j.rinp.2020.102930.
15. Shin, H.; Heo, N.; Park, J.; Seo, I.; Yoo, J. All-dielectric structure development for electromagnetic wave shielding using a systematic design approach. *Appl. Phys. Lett.* **2017**, *110*, 021908. https://doi.org/10.1063/1.4974162.
16. Devendran, M.; Beno, A.; Kannan, K.; Dhamodaran, M.; Sorathiya, V.; Patel, S.K. Numerical investigation of cross metamaterial shaped ultrawideband solar absorber. *Opt. Quantum Electron.* **2022**, *54*, 323. https://doi.org/10.1007/s11082-022-03670-3.
17. Sun, R.; Li, W.Y.; Meng, T.H.; Zhao, G.Z. Design and optimization of terahertz metamaterial sensor with high sensing performance. *Opt. Commun.* **2021**, *494*, 127051. https://doi.org/10.1016/j.optcom.2021.127051.
18. Han, G.F.; Bai, R.P.; Jin, X.R.; Zhang, Y.Q.; An, C.S.; Lee, Y. Dual-band unidirectional reflectionless propagation in metamaterial based on two circular-hole resonators. *Materials* **2018**, *11*, 2353. https://doi.org/10.3390/ma11122353.
19. Lv, Y.L.; Xu, D.Y.; Yin, F.H.; Yang, Y.L.; Zhang, Y.Q.; An, C.S.; Jin, X.R. A versatile meta-device for linearly polarized waves in terahertz region. *Phys. Scripta* **2024**, *99*, 025517. https://doi.org/10.1088/1402-4896/ad1a36.

 doi:10.20944/preprints202504.1857.v1

20. Li, Z.T.; Li, X.; Liu, G.D.; Wang, L.L.; Lin, Q. Analytical investigation of unidirectional reflectionless phenomenon near the exceptional points in graphene plasmonic system. *Opt. Express* **2023**, *31*, 30458–30469. https://doi.org/10.1364/OE.499904.
21. Park, H.; Lee, J.; Shim, J.; Son, H.; Park, J.; Baek, S.; Kim, T.T. Broadband metamaterial polarizers with high extinction ratio for high-precision terahertz spectroscopic polarimetry. *APL Photonics* **2024**, *9*, 110807. https://doi.org/10.1063/5.0228119.
22. Singh, R.; Plum, E.; Menzel, C.; Rockstuhl, C.; Azad, A.; Cheville, R.; Lederer, F.; Zhang, W.; Zheludev, N. Terahertz metamaterial with asymmetric transmission. *Phys. Rev. B* **2009**, *80*, 153104. https://doi.org/10.1103/PhysRevB.80.153104.
23. Qureshi, U.U.R.; Deng, B.; Wu, X.D.; Xiong, C.J.; Jalal, A.; Khan, M.I.; Hu, B. Chiral terahertz metasurface with asymmetric transmission, polarization conversion and circular dichroism. *Opt. Express* **2024**, *32*, 32836–32848. https://doi.org/10.1364/OE.529311.
24. Xu, D.Y.; Lv, Y.L.; Zhang, Y.Q.; Jin, X.R. Unidirectional reflectionlessness, asymmetric reflection, and asymmetric transmission with linear and circular polarizations in terahertz metamaterial. *Aip Adv.* **2024**, *14*, 095121. https://doi.org/10.1063/5.0221687.
25. Yin, F.H.; Zhang, Y.Q.; Jin, X.R. Manipulation of unidirectional reflectionlessness and asymmetric transmissionlessness in terahertz metamaterials. *Opt. Commun.* **2023**, *533*, 129309. https://doi.org/10.1016/j.optcom.2023.129309.
26. Nguyen, T.Q.H.; Nguyen, T.M.; Nguyen, H.Q. High efficient bi-functional metasurface with linear polarization conversion and asymmetric transmission for terahertz region. *J. Opt.* **2025**, *27*, 015104. https://doi.org/10.1088/2040-8986/ad8c5f.
27. Ahmed, A.; Cao, Q.S.; Khan, M.I.; Shah, G.; Ahmed, F.; Khan, M.I.; Abidin, Z.U. An angular stable ultra-broadband asymmetric transmission chiral metasurface with efficient linear-polarization conversion. *Phys. Scripta* **2024**, *99*, 035519. https://doi.org/10.1088/1402-4896/ad25d1.
28. Li, Y.; Zeng, L.; Zhang, H.; Zhang, D.; Xia, K.; Zhang, L. Multifunctional and tunable metastructure based on VO2 for polarization conversion and absorption. *Opt. Express* **2022**, *30*, 34586–34600. https://doi.org/10.1364/OE.470910.
29. Wang, Q.Z.; Zhang, H.W.; Ren, G.J.; Xue, L.F.; Yao, J.Q. Photosensitive silicon-based tunable multiband terahertz absorber. *Opt. Commun.* **2022**, *523*, 128681. https://doi.org/10.1016/j.optcom.2022.128681.
30. Song, Z.Y.; Zhang, J.H. Achieving broadband absorption and polarization conversion with a vanadium dioxide metasurface in the same terahertz frequencies. *Opt. Express* **2020**, *28*, 12487–12497. https://doi.org/10.1364/OE.391066.
31. Zhao, Y.J.; Yang, R.C.; Wang, Y.X.; Zhang, W.M.; Tian, J.P. VO 2-assisted multifunctional metamaterial for polarization conversion and asymmetric transmission. *Opt. Express* **2022**, *30*, 27407–27417. https://doi.org/10.1364/OE.462813.
32. Xu, B.L.; Zhong, R.B.; Liang, Z.K.; Fang, Z.; Fang, J.H.; Zhang, H.M.; Wu, Z.H.; Zhang, K.C.; Hu, M.; Liu, D.W. A tunable multifunctional terahertz asymmetric transmission device hybrid with vanadium dioxide blocks. *Front. Mater.* **2022**, *9*, 881229. https://doi.org/10.3389/fmats.2022.881229.
33. Yuan, W.X.; Zhang, Y.Q.; Jin, X.R. Tunable unidirectional reflectionlessness based on vanadium dioxide in a non-Hermitian metamaterial. *Phys. Scripta* **2024**, *99*, 125550. https://doi.org/10.1088/1402-4896/ad9096.
34. Chen, D.B.; Yang, J.B.; Huang, J.; Bai, W.; Zhang, J.J.; Zhang, Z.J.; Xu, S.Y.; Xie, W.L. The novel graphene metasurfaces based on split-ring resonators for tunable polarization switching and beam steering at terahertz frequencies. *Carbon* **2019**, *154*, 350–356. https://doi.org/10.1016/j.carbon.2019.08.020.
35. Sajjad, M.; Kong, X.K.; Liu, S.B.; Ahmed, A.; Rahman, S.U.; Wang, Q. Graphene-based THz tunable ultra-wideband polarization converter. *Phys. Lett. A* **2020**, *384*, 126567. https://doi.org/10.1016/j.physleta.2020.126567.
36. Yang, Y.P.; Fan, S.T.; Zhao, J.J.; Xu, J.Z.; Zhu, J.F.; Wang, X.R.; Qian, Z.F. A multi-functional tunable terahertz graphene metamaterial based on plasmon-induced transparency. *Diam. Relat. Mater.* **2024**, *141*, 110686. https://doi.org/10.1016/j.diamond.2023.110686.
37. Xu, J.; Tang, J.; Cheng, Y.; Chen, M.; Wang, H.X.; Xiong, J.F.; Wang, T.R.; Wang, S.Z.; Zhang, Y.D.; Wen, H.; et al. Multifunctional analysis and verification of lightning-type electromagnetic metasurfaces. *Opt. Express* **2022**, *30*, 17008–17025. https://doi.org/10.1364/OE.458412.
38. Wu, R.L.; Li, J.S. Bi-directional multi-function terahertz metasurface. *Opt. Commun.* **2023**, *529*, 129105. https://doi.org/10.1016/j.optcom.2022.129105.
39. Zhu, W.C.; Jiang, H.; Zhao, S.L.; Zhang, H.; Zhao, W.R. Large and active circular dichroism in a photosensitive silicon based metasurface. *J. Opt.* **2024**, *26*, 035101. https://doi.org/10.1088/2040-8986/ad21d9.

 doi:10.20944/preprints202504.1857.v1

40. Cai, X.S.; Xiao, Z.Y.; Zheng, Q.; Liu, Y.L.; Huang, J.Z.; Zhu, J.W.; Guo, C.P. Monolayer actively tunable dual-frequency switch based on photosensitive silicon metamaterial. *Opt. Commun.* **2024**, *562*, 130557. https://doi.org/10.1016/j.optcom.2024.130557.
41. Wang, Q.Z.; Liu, S.Y.; Ren, G.J.; Zhang, H.W.; Liu, S.C.; Yao, J.Q. Multi-parameter tunable terahertz absorber based on graphene and vanadium dioxide. *Opt. Commun.* **2021**, *494*, 127050. https://doi.org/10.1016/j.optcom.2021.127050.
42. Zhou, Q.G.; Li, Y.Z.; Wu, T.T.; Qiu, Q.X.; Duan, J.X.; Jiang, L.; Mao, W.C.; Yao, N.J.; Huang, Z.M. Terahertz metasurface modulators based on photosensitive silicon. *Laser Photonics Rev.* **2023**, *17*, 2200808. https://doi.org/10.1002/lpor.202200808.
43. Jiang, X.X.; Xiao, Z.Y.; Wang, X.W.; Cheng, P. Integrated metamaterial with the functionalities of an absorption and polarization converter. *Appl. Opt.* **2023**, *62*, 3519–3527. https://doi.org/10.1364/AO.484368.
44. Schubert, E.F.; Kim, J.K.; Xi, J.Q. Low-refractive-index materials: A new class of optical thin-film materials. *phys. stat. sol. (b)* **2007**, *244*, 3002–3008. https://doi.org/10.1002/pssb.200675603.
45. Zhang, X.; Wang, G.; Liu, J.; Zuo, S.; Li, M.; Yang, S.; Jia, Y.; Gao, Y. Switchable and tunable terahertz metamaterial based on vanadium dioxide and photosensitive silicon. *Nanomaterials* **2023**, *13*, 2144. https://doi.org/10.3390/nano13142144.
46. Cheng, Y.Z.; Gong, R.Z.; Zhao, J.C. A photoexcited switchable perfect metamaterial absorber/reflector with polarization-independent and wide-angle for terahertz waves. *Opt. Mater.* **2016**, *62*, 28–33. https://doi.org/10.1016/j.optmat.2016.09.042.
47. Li, J.S.; Li, X.J. Switchable tri-function terahertz metasurface based on polarization vanadium dioxide and photosensitive silicon. *Opt. Express* **2022**, *30*, 12823–12834. https://doi.org/10.1364/OE.454240.
48. Luo, B.; Qi, Y.P.; Zhou, Z.H.; Shi, Q.; Wang, X.X. Switchable bi-functional metasurface for absorption and broadband polarization conversion in terahertz band using vanadium dioxide and photosensitive silicon. *Nanotech.* **2024**, *35*, 195205. https://doi.org/10.1088/1361-6528/ad22ae.
49. Wang, J.Y.; Yang, R.C.; Li, Z.H.; Tian, J.P. Reconfigurable multifunctional polarization converter based on asymmetric hybridized metasurfaces. *Opt. Mater.* **2022**, *124*, 111953. https://doi.org/10.1016/j.optmat.2021.111953.
50. Wang, X.W.; Xiao, Z.Y.; Wang, X.Y.; Miao, X.; Jiang, X.X.; Li, A.Q. Tunable and switchable common-frequency broadband terahertz absorption, reflection and transmission based on graphene-photosensitive silicon metamaterials. *Opt. Commun.* **2023**, *541*, 129555. https://doi.org/10.1016/j.optcom.2023.129555.
51. Wang, G.; Zuo, S.Y.; Liu, J.; Zhang, X.; Li, M.C.; Yang, S.; Jia, Y.; Gao, Y.C. Difunctional terahertz metasurface with switchable polarization conversion and absorption by VO 2 and photosensitive silicon. *Phys. Chem. Chem. Phys.* **2023**, *25*, 19719–19726. https://doi.org/10.1039/D3CP01649H.
52. Cui, Y.; Wang, X.; Ren, B.; Jiang, H.; Jiang, Y. High-efficiency and tunable circular polarization selectivity in photosensitive silicon-based zigzag array metasurface. *Opt. Laser Technol.* **2022**, *156*, 108453. https://doi.org/10.1016/j.optlastec.2022.108453.
53. Liu, H.; Zhao, J.; Chen, C.; Gao, P.; Dai, Y.; Lu, X.; Wan, Y.; Zhao, S.; Wang, X. Switchable multifunctional metasurface based on electromagnetically induced transparency and photosensitive silicon. *Opt. Quantum Electron.* **2024**, *56*, 176. https://doi.org/10.1007/s11082-023-05807-4.
54. Yuan, S.; Yang, R.; Xu, J.; Wang, J.; Tian, J. Photoexcited switchable single-/dual-band terahertz metamaterial absorber. *Mater. Res. Express.* **2019**, *6*, 075807. https://doi.org/10.1088/2053-1591/ab1962.
55. Chen, H.T.; O'hara, J.F.; Azad, A.K.; Taylor, A.J.; Averitt, R.D.; Shrekenhamer, D.B.; Padilla, W.J. Experimental demonstration of frequency-agile terahertz metamaterials. *Nature Photon.* **2008**, *2*, 295–298. https://doi.org/10.1038/nphoton.2008.52.
56. Shabanpour, J.; Beyraghi, S.; Cheldavi, A. Ultrafast reprogrammable multifunctional vanadium-dioxide-assisted metasurface for dynamic THz wavefront engineering. *Sci. Rep.* **2020**, *10*, 8950. https://doi.org/10.1038/s41598-020-65533-9.